Simple Models of Directly Measured Energy Landscapes for Different Shaped Particles in Nonuniform AC Electric Fields

*Lechuan Zhang,† Alec J. Pellicciotti,† Rachel S. Hendley, Xiao Wang, Michael A. Bevan**
Chemical & Biomolecular Engr., Johns Hopkins Univ., Baltimore, MD, 21218 USA

Abstract

We report direct measurements of potential energy landscapes for different shaped colloidal particles interacting with nonuniform AC electric fields. Epoxy particle shapes investigated include disks, ellipses, squares, rectangles, and rhombuses, which are all part of the superelliptical prism shape class and are chosen to systematically vary particle anisotropy and corner features. The measurement configuration consists of non-interacting single particles sedimented onto microscope slides within electric fields between parallel coplanar electrodes. Thermally sampled positions and orientations of single particles in nonuniform fields are tracked in an optical microscope, and measured potential energy landscapes are obtained via Boltzmann inversions. We develop a new analytically simple model that captures all measured energy landscapes for superelliptical prism shaped colloidal particles with electrostatic double layers. The model recovers known validated potentials for spherical and ellipsoidal particles, and therefore captures energy landscapes for a variety of different colloidal particle sizes, shapes, and materials reported in prior studies.

keywords: induced dipoles | dipole-field potentials | Boltzmann inversion | anisotropic particles | superelliptical prisms

Introduction

Dipolar interactions between polarizable colloidal components are ubiquitous and essential to the behavior and properties of particle-based materials in a diverse range of phenomena and applications. Permanent, induced, and instantaneous dipolar interactions are essential to the behavior and properties of molecular systems in the form of van der Waals interactions, which also operate between colloidal particles.[1-3] Electric, magnetic, and optical fields can induce dipoles in colloidal materials with suitable polarizabilities, and thus can be used as "tweezers" by producing net trapping forces on particles at field maxima or mimina.[4-9] Fields can be shaped in 2D[10] or 3D[11] to control forces and torques on different shaped single particles,[12] many single particles at multiple field maxima/minima (as in holographic optical tweezers),[11] and entire particle ensembles residing within nonuniform fields.[13] Understanding induced dipolar interactions provides fundamental understanding of material interactions with electromagnetic fields and practically enables high fidelity control over microscopic materials and devices. Colloidal particles with induced dipoles interacting with nonuniform external fields is practically relevant to numerous traditional applications (e.g., electro- and magneto rheological fluids) and emerging technologies (single particle micro-manipulation, sensing, separations, assembly, etc.).[7, 14-16]

Understanding forces on particles in AC electric fields has been studied for a long time as summarized in textbooks dedicated to this subject.[17-19] A common basic case to consider is AC electric field mediated polarization of spherical colloidal particles with core material dielectric

*To whom correspondence should be addressed. email: mabevan@jhu.edu
† These authors contributed equally to this work.

properties[20] and a polarizable electrostatic double layer in aqueous media.[21-23] The resulting time averaged force in this case arises from the particle-medium polarization mismatch,[19] where particle conductivity can be modeled as a surface conductance due to electrostatic double layer contributions.[21-23] The frequency dependent force on spherical colloids in nonuniform AC electric fields has been validated primarily from the steady translational velocity of particles against a known hydrodynamic drag force, which is commonly referred to as dielectrophoresis.[19] Other measurements based on force balances against known forces include optical tweezer measurements.[24-25] An alternative approach is to directly measure thermal sampling of single spherical colloids in nonuniform AC electric fields, where a Boltzmann inversion yields the potential energy landscape,[26-27] and its spatial derivatives yield the force (without requiring knowledge of an independent force; e.g. hydrodynamic, optical, etc.). While details of polarization models for specific materials and field conditions are still the subject of ongoing study, measurements and models agree sufficiently to suggest dominant physics are reasonably well understood for spherical colloids in nonuniform AC electric fields.

For non-spherical colloids in AC electric fields, open questions remain about the forces and torques on particles with arbitrary shapes (polyhedral, anisotropic), nonuniform material properties (Janus, birefringent), and field conditions (voltage, frequency, shape, time dependence).[28-29] Dielectric ellipsoids are perhaps the simplest perturbation to spherical particles and the most studied anisotropic particles in both experiments and theory. Theoretical ellipsoid models based on electrostatics,[20] including contributions from electrostatic double layers[21-22] and core-shell material properties,[30] have been applied to model forces and torques that control position and orientation of a number of anisotropic objects including polymer chains, DNA, viruses, particle chains, and cells.[17-19] Although many of these objects are not ellipsoidal in shape, first principles models have not been developed to consider additional complexities associated with more diverse shapes. Ellipsoid models are also quite complex and have been simplified to become somewhat more usable for specific cases of certain material properties, field conditions, and limited scenarios where particles only align with dominant field vectors.[17]

Direct measurements of forces and torques on non-spherical particles in AC electric fields and their comparison with rigorous expressions are limited. In many cases, the comparison is semi-quantitative and indirect (*e.g.*, macroscopic birefringence measurements, see references within Ref.[22]). Single particle dipolar torque measurements are generally performed by electro-rotation experiments that involve a torque balance against a hydrodynamic drag torque (analogous to force balances to measure dipole-field force).[17-19] Such torque balances are often limited by knowledge of the hydrodynamic torque, which can be complex for anisotropic particle adjacent to surfaces,[31-32] or when particle's electrostatic double layers overlap with underlying surface[33] (as particles sedimented on a microscope slide). As with spherical particles, an alternative approach can be used that avoids requiring knowledge of hydrodynamic drag forces and torques; by observing an anisotropic particle's equilibrium thermal sampling of different positions and orientations within nonuniform fields, a Boltzmann inversion directly yields the multi-dimensional energy landscape[12] (and partial derivatives with respect to position and orientation yield forces and torques). Such measured potential energy landscapes have indicated up to 12 states of position and orientation for tri-axial particles in nonuniform AC electric fields,[34] which indicates significant potential for micromanipulation of colloidal objects. Despite the promise of this measurement approach, it has seen limited use, perhaps as a result of the difficulty of determining conditions where particles thermally sample different equilibrium states (without prior knowledge of energy landscapes).

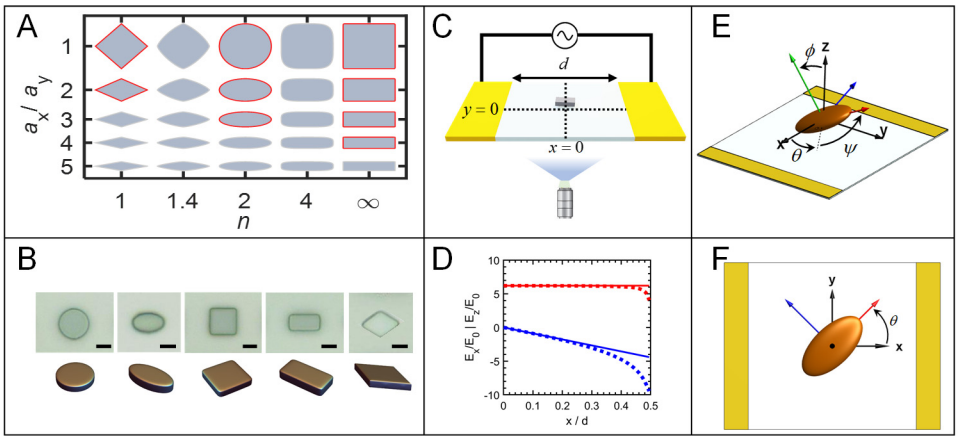

Fig. 1. Overview of particle shapes, particle and lab coordinates, and electric field shape. (A) Superellipse shapes vs. aspect ratio, $s=a_x/a_y$, and the corner parameter, n (Eq. (1)), where red outline indicates approximate shapes measured in this work. **(B)** (top) optical microscope images of fabricated SU-8 superelliptical prisms (4 μm scale bars), and (bottom) 3D renderings. **(C)** Schematic of rectangular prism between parallel coplanar electrodes (gold indicates electrode, white surface represents glass substrate). **(D)** Electric field components in x and z directions. **(E)** Schematic of 6D position and orientation of tri-axial (scalene) ellipsoid between parallel electrode with laboratory coordinates (x, y, z) and Euler angles (θ, φ, ψ). **(F)** Schematic of same ellipsoid in panel E confined to 2D translation in x, y and rotation in θ.

To address open challenges in measuring and modeling different shaped colloids in nonuniform fields, in this work, we first directly measure dipole-field energy landscapes for systematically varying particle shapes in nonuniform AC electric fields. We then develop a simple model that quantifies all measured energy landscapes and their features. The investigated particle shapes are all from the superelliptical prism shape class (**Fig. 1A**). This particle shape class allows for systematic variations of disks into elliptical shapes, and an additional parameter to continuously tune corners on squares, rectangles, and rhombuses. Specific particle shapes investigated include circular, elliptical, square, rectangular, and rhombic prism particles, which represent many practical particle shapes of interest (**Fig. 1B**). Micron sized epoxy particles are synthesized via photolithography, and their positions and orientations are tracked via optical microscopy between coplanar parallel electrodes (**Fig. 1C**). As in our prior studies on spheres[27] and a single anisotropic particle shape,[12] a Boltzmann inversion of measured position and orientation histograms yield measured potential energy landscapes, with no assumptions (other than the validity of Boltzmann's equation). We adapt and extend a 3D model for tri-axial (scalene) ellipsoids (**Figs. 1E**)[34] by analytically reducing it for 2D systems (**Figs. 1F**) and then finally determine approximations to yield a new simple, generalizable potential capturing all measurements in this work and a broad range of particle sizes, shapes, and materials from prior studies.

Theory

Superelliptical Prisms

Particle shapes investigated in this work are all superelliptical prisms, where the equation of their projected 2D perimeter is given by,

$$\left|x/a_x\right|^n + \left|y/a_y\right|^n = 1 \tag{1}$$

where a_x and a_y are major and minor radii, aspect ratio is $s=a_x/a_y$, and n determines particle shape.

Superellipse shapes include (**Fig. 1**) disks (n=2, s=1), ellipses (n=2, s>1), squares ($n\to\infty$, s=1), rectangles ($n\to\infty$, s>1), and rhombuses (n=1, s>1). Superelliptical prism particles of thickness $2a_z$ have volumes of,

$$v_{\mathrm{p,SEP}} = 2a_{\mathrm{z}}A_{SE} = 8a_{\mathrm{z}}a_{\mathrm{x}}a_{\mathrm{y}}\left[\Gamma\left(1+n^{-1}\right)\right]^2\left[\Gamma\left(1+2n^{-1}\right)\right]^{-1} \tag{2}$$

where Γ is the gamma function. For comparison, an ellipsoid with the same radii has a volume,

$$v_{\mathrm{p,E}} = \left(4/3\right)\pi a_{\mathrm{x}}a_{\mathrm{y}}a_{\mathrm{z}} \tag{3}$$

3D Ellipsoidal Dipole-Field Potential

The position and orientation dependent potential energy for a dielectric ellipsoid in a nonuniform electric field is given by,[20, 34]

$$u^{\mathrm{df}}\left(x,y,z,\theta,\phi,\psi\right) = -\left(3/2\right)\varepsilon_{\mathrm{m}}v_{\mathrm{p}}\mathbf{f}_{\mathrm{cm}}\cdot\left[\mathbf{A}\left(\theta,\phi,\psi\right)\cdot\mathbf{E}\left(x,y,z\right)\right]^{\circ 2} \tag{4}$$

where ε_{m} is the medium permittivity and v_p is particle volume. The particle center position (x, y, z) and orientation (θ, φ, ψ) in laboratory coordinates are defined in **Fig. 1E**. Particle and medium material properties appear in the Clausius–Mossotti factor, $\mathbf{f}_{\mathrm{cm}}$, which has components,

$$f_{\mathrm{cm,k}} = \mathrm{Re}\left[\frac{1}{3}\frac{\tilde{\varepsilon}_{\mathrm{p}}-\tilde{\varepsilon}_{\mathrm{m}}}{\tilde{\varepsilon}_{\mathrm{m}}+\left(\tilde{\varepsilon}_{\mathrm{p}}-\tilde{\varepsilon}_{\mathrm{m}}\right)L_{\mathrm{k}}}\right] \tag{5}$$

$$\tilde{\varepsilon}_m = \varepsilon_m - i\sigma_m/\omega,\ \tilde{\varepsilon}_{p,r_A} = \varepsilon_p - i\sigma_p/\omega$$

where the index k indicates the particle axes (x, y, z), p and m subscripts indicate particle and medium properties, σ is conductivity, ω is field frequency, and the depolarization factor, L_{k}, is,

$$L_k = \frac{a_x a_y a_z}{2}\int_0^\infty \frac{1}{\left(s+a_k^2\right)\sqrt{\left(s+a_x^2\right)\left(s+a_y^2\right)\left(s+a_z^2\right)}}\,ds \tag{6}$$

and the electric field, **E,** is transformed from laboratory (E_{x}, E_{y}, E_{z}) to particle coordinates by,

$$\mathbf{A} = \begin{pmatrix} \cos\psi\cos\theta-\cos\phi\sin\theta\sin\psi & \cos\psi\sin\theta+\cos\phi\cos\theta\sin\psi & \sin\psi\sin\phi \\ -\sin\psi\cos\theta-\cos\phi\sin\theta\cos\psi & -\sin\psi\sin\theta+\cos\phi\cos\theta\cos\psi & \cos\psi\sin\phi \\ \sin\phi\sin\theta & -\sin\phi\cos\theta & \cos\phi \end{pmatrix} \tag{7}$$

where θ, ϕ, and ψ are Euler angles (**Fig. 1E**).

2D Simplification of 3D Ellipsoidal Dipole-Field Potential

For ellipsoidal particles within quasi-2D configurations where out-of-plane translation (z is nearly constant) and out-of-plane rotation is minimal (ϕ=ψ=0), Eqs. (4)-(7) can be analytically simplified. The criteria for satisfying quasi-2D conditions are based on the sedimentation equilibrium gravitational length being less than particle dimensions[35] and the gravitational penalty for out-of-plane rotation being significantly greater than kT (see prior work for quantitative models based on 6-dimensional potential energy landscapes using Eq. (4)[34]). By letting ϕ=ψ=0, the transformation matrix in Eq. (7) simplifies to,

$$\mathbf{A} = \begin{pmatrix} \cos\theta & \sin\theta & 0 \\ -\sin\theta & \cos\theta & 0 \\ 0 & 0 & 1 \end{pmatrix} \tag{8}$$

By inserting Eq. (8) into Eq. (4), and for coplanar electrodes where $E_y = 0$, Eq. (4) simplifies to a two-dimensional potential energy landscape as,

$$u^{\mathrm{df}}(x,\theta) = -(3/2)\varepsilon_{\mathrm{m}} v_{\mathrm{p}} \left[f_{\mathrm{cm,x}} E_x^2(x)\cos^2\theta + f_{\mathrm{cm,y}} E_x^2(x)\sin^2\theta + f_{\mathrm{cm,z}} E_{\mathrm{z}}^2(x) \right] \tag{9}$$

By limiting analysis to particles predominantly aligned with the field direction (θ=0), and localized near the electric field minimum (x=0) where E_{x} is nearly spatially invariant, the potential in Eq. (9) relative to the reference state of (x=0, θ=0) simplifies (using trigonometric identities) to,

$$u^{\mathrm{df}}(x,\theta) - u^{\mathrm{df}}(0,0) = -(3/2)\varepsilon_{\mathrm{m}} v_{\mathrm{p}} \left[\left(f_{\mathrm{cm,y}} - f_{\mathrm{cm,x}} \right) E_x^2 \sin^2\theta + f_{\mathrm{cm,z}} E_{\mathrm{z}}^2(x) \right] \tag{10}$$

Semi-Empirical 2D Superelliptical Prism Dipole-Field Potential

Beyond mathematical simplification of Eq. (4) to obtain Eqs. (9) and (10) for specific conditions, the functional form of the potential energy landscape can be written more simply as,

$$u^{\mathrm{df}}(x,\theta) - u^{\mathrm{df}}(0,0) = -P^{df} \left[f_\theta E_{\mathrm{x}}^2 \sin^2\theta + f_{\mathrm{x}} E_{\mathrm{z}}^2(x) \right] \tag{11}$$

based on multiplying the pre-factor in Eq. (10) by the spherical particle Clausius–Mossotti factor, f_{cm}, dividing each term within the parentheses by f_{cm}, and defining substitutions as,

$$P^{\mathrm{df}} = (3/2)\varepsilon_{\mathrm{m}} v_{\mathrm{p}} f_{\mathrm{cm}},\ f_{\mathrm{cm}} = \mathrm{Re}\left[\frac{\tilde{\varepsilon}_p - \tilde{\varepsilon}_m}{3\tilde{\varepsilon}_m + \left(\tilde{\varepsilon}_p - \tilde{\varepsilon}_m \right)} \right],\ f_\theta = \left(f_{\mathrm{cm,y}} - f_{\mathrm{cm,x}} \right) f_{\mathrm{cm}}^{-1},\ f_{\mathrm{x}} = f_{\mathrm{cm,z}} f_{\mathrm{cm}}^{-1} \tag{12}$$

where f_{cm} is obtained with a_x=a_y=a_z in Eqs. (5) and (6). The form of Eq. (11) is valid for 2D ellipsoids with major axes oriented with electric fields at field minima and also recovers the standard spherical dipole-field potential (for f_{x}=1, f_θ=0).[8, 26-27]

The dipole-field scalar potential energy landscape in Eq. (11) can be used to specify functional forms for time-averaged dipole-field forces, F, and torques, T, based on partial derivatives with respect to position and orientation given by,

$$F = -\frac{\partial u^{\mathrm{df}}(x,\theta)}{\partial x} = 2P^{\mathrm{df}} \left[f_\theta \sin^2\theta E_x \frac{\partial E_x(x)}{\partial x} + f_{\mathrm{x}} E_z \frac{\partial E_z(x)}{\partial x} \right] \approx 2P^{\mathrm{df}} f_{\mathrm{x}} \left(8.9 E_0/\pi d \right)^2 x \tag{13}$$

$$T = -\frac{\partial u^{\mathrm{df}}(x,\theta)}{\partial \theta} = 2P^{\mathrm{df}} f_\theta E_x^2 \sin\theta\cos\theta \approx 2P^{\mathrm{df}} f_\theta \left(6.2 E_0/\pi \right)^2 \sin\theta\cos\theta \tag{14}$$

where the right hand side is for approximate time-averaged coplanar electrode field components (Eq. (15)).

Coplanar Electrode Electric Field

The electric field between semi-infinite, thin-film, coplanar electrodes has components given by an analytical solution,[36] which can be approximated by,

$$E_x = \frac{2E_0}{\pi}\left[\tan^{-1}\left(\frac{\sin\hat{x}}{\sinh\hat{z}}\right)-\tan^{-1}\left(\frac{\cos\hat{x}}{\sinh\hat{z}}\right)\right]\approx E_0\left(6.2/\pi\right)$$

$$E_z = \frac{E_0}{\pi}\left[\ln\left(\frac{\cosh\hat{z}+\cos\hat{x}}{\cosh\hat{z}-\cos\hat{x}}\frac{\cosh\hat{z}+\sin\hat{x}}{\cosh\hat{z}-\sin\hat{x}}\right)\right]\approx -E_0\left(8.9/\pi\right)\left(x/d\right) \quad (15)$$

$$\hat{x}=\pi\left(x+d\right)/2d+\pi/4,\ \ \hat{z}=\pi z/2d$$

where $E_0 = (8^{-0.5})V_{pp}/d$, where the factor ($8^{-0.5}$) accounts for time-averaging a sinusoidal waveform (in contrast, the factor is ($12^{-0.5}$) for a triangular waveform and 1 for a DC field), d is the electrode gap, and $z=a_z+h_m$, where h_m is the most probable height (via a force balance in the laboratory z-coordinate).[37] The approximate field components are accurate within 5% for $x/d<0.25$, which is sufficient for particle thermal sampling about the electric field minimum at $x=0$.

Energy Landscapes & Probability Distributions

The potential energy of an anisotropic particle in a nonuniform electric field (Eq. (4)) is a function of up three translational degrees of freedom (x, y, z) and three rotational degrees of freedom (ϕ, θ, ψ). Analysis of all dimensions as well as methods to analyze cases of reduced dimensionality for comparison with experiment have previously been reported.[12, 34] For particles that sample 2D coordinates within a plane (x, y, θ), and when the potential energy has no y-dependence (as in Eqs. (9)-(11)), the probability of sampling different positions and orientations is related to their relative potential energies via Boltzmann's equation as,

$$p\left(x,\theta\right)=p\left(0,0\right)\exp\left[-\left(u^{df}\left(x,\theta\right)-u^{df}\left(0,0\right)\right)/kT\right] \quad (16)$$

where (x=0, θ=0) are the potential energy reference coordinates as already noted. Eq. (16) can be inverted to obtain relative potential energies from measured histograms (*i.e.*, $p(x,\theta)$) as,

$$u\left(x,\theta\right)-u\left(0,0\right)=kT\ln\left[p\left(0,0\right)/p\left(x,\theta\right)\right] \quad (17)$$

The 2D energy landscapes obtained either from measurements via Eq. (17) or the model in Eq. (11) can be projected to consider only orientation or position dependent probabilities as,

$$\left\langle p\left(\theta\right)\right\rangle=\left(2/d\right)\int_0^{d/2}p\left(x,\theta\right)dx,\ \ \left\langle p\left(x\right)\right\rangle=\left(2/\pi\right)\int_0^{\pi/2}p\left(x,\theta\right)d\theta \quad (18)$$

which can be inverted to obtain average 1D x or θ dependent energy landscapes as,

$$\left\langle u\left(\theta\right)\right\rangle=kT\ln\left(\left\langle p\left(0\right)\right\rangle/\left\langle p\left(\theta\right)\right\rangle\right),\ \ \left\langle u\left(x\right)\right\rangle=kT\ln\left(\left\langle p\left(0\right)\right\rangle/\left\langle p\left(x\right)\right\rangle\right) \quad (19)$$

Materials & Methods

Particle Fabrication. Anisotropic superelliptical prism epoxy particles (all chemicals from MicroChem) were fabricated using photolithography with similar methods to prior studies.[38] In brief, Omnicoat and SU-8 2002 were spin coated at 3000 rpm on a silicon wafer followed by heat treatment. A particle shape photomask was used to pattern particles on a wafer with a UV exposure energy of 80 mJ/cm^2 and then heat-treated. Uncured excess SU-8 was removed by immersing in PG Developer and isopropyl alcohol. Particle dimensions were confirmed with a laser-scanning microscope (Keyence). Particles on wafers were treated with 50% sulfuric acid to yield negative

surface charge and cleaned with deionized water. Particles were released by PG Remover and cleaned with isopropyl alcohol and deionized water. These steps yield maximum negative surface charge to prevent aggregations and irreversible deposition on electrodes.[38-39]

Microscopy and Particle Tracking. The microscopy cell was similar to prior studies.[26-27, 34, 37, 40] An O-ring (McMaster-Carr) was placed on microfabricated interdigitated gold electrodes patterned on a glass slide. Particles were dispersed and pipetted into the O-ring to give ~3-5 particles in the imaging window. Electrodes were connected to a function generator (Agilent 33220A) to apply sinusoidal AC fields with 3 V peak-to-peak voltage and 5 MHz frequency. Particles were imaged with an inverted microscope (Zeiss) using a 40× objective. Videos were captured at 9 frames/s for 18 minutes and ~10^4 total frames using a CCD camera (Hamamatsu, Orca-ER) and Streampix (Norpix) software. Particle centroid position (x,y) and long-axis orientation (θ) were tracked using previously reported MATLAB algorithms.[12]

Results & Discussion

Circular Prisms (*Disks*)

We first investigate the simplest superelliptical prism shape (**Fig. 2A**), which is a circular prism, or more simply a disk (a_x=a_y=4 μm, a_z=0.85 μm). In this case, and for all superelliptical prism shapes investigated in this work, the two longest radii align parallel to the microscope slide. We have previously shown for SU-8 particles with the same density and similar dimensions that the gravitational potential energy change associated with these axes rotating out of the quasi 2D plane parallel to the microscope slide is too high and practically suppressed.[12, 31] Furthermore, we have shown that finite thermal sampling of out-of-plane elevations and orientations are practically

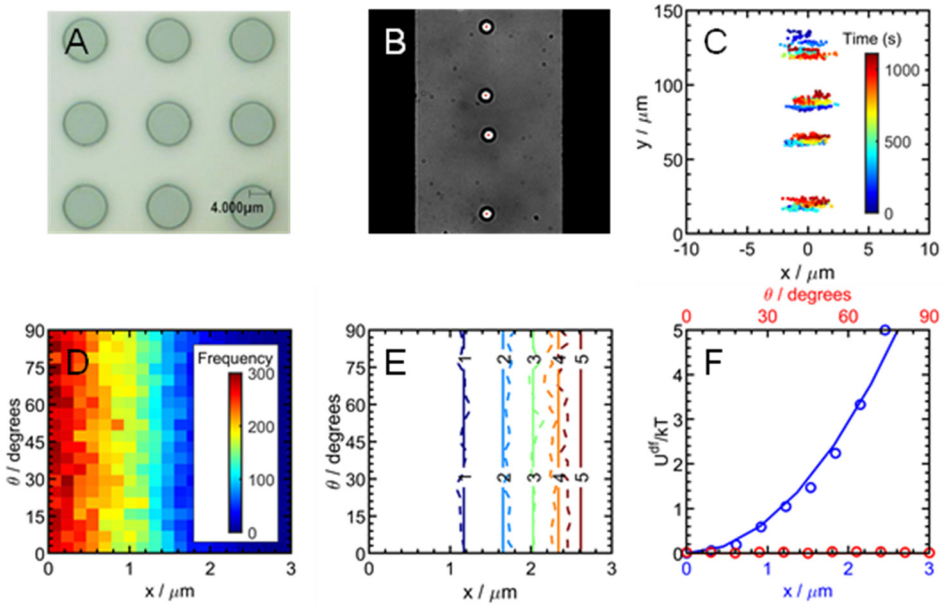

Fig. 2. Circular prism (disk) particle dipole-field energy landscapes. (A) SU-8 particle image (a_x=4 μm, a_y=4 μm, a_z=0.85 μm, n=2). **(B)** Video microscopy image showing tracked particle centers (red points) within electrode gap (100 μm) for 5 MHz, 10.6 V/mm AC electric field. **(C)** Particle center trajectories. **(D)** Histogram of (x, θ) distribution relative to electrode gap center and field orientation (see Fig. 1). **(E)** Contour plot with 1 kT spacing for (dashed) measured 2D dipole-field energy landscape and (solid) Eq. (11) with fit f_x, f_θ = parameters in Table 2. **(F)** Projection of 2D energy landscapes in (E) into 1D x (blue) and θ (red) landscapes for (points) measured potentials and (lines) Eq. (11).

averaged to be the same as particles with constant 2D coordinates (*i.e.*, $z=h_m+a_z$, $\psi=\phi=0$).[34] The 2D projected shape of disk particles is not easily distinguishable from spherical particles,[27] although their volumes clearly differ for the same radius.

For all shapes studied here, we use a peak-to-peak voltage of V_{pp}=3 V (E_0=10.6 V/mm), which limits thermal translation and rotation to small region at the electric field minimum while also allowing sufficient statistics to be obtained in a relatively short time over an appreciable spatial extent to construct energy landscapes. Practically, much lower voltages allow more translational and rotational diffusion over greater distances and longer times and thus take longer to obtain statistically significant histograms. In contrast, applying much higher voltages causes particles to sample a very narrow range of positions and orientations, which can be harder to spatially resolve. As a result, we choose a moderate voltage to balance these two competing effects. For example, while an electric tweezer application might aim to localize particles and suppress motion, here thermal sampling aids analysis and sampling of potential energy landscapes via Eq. (17). All experiments use a field frequency of 5 MHz, which causes the longest axis of all particle shapes to align with the electric field and localize at the electric field minimum (to satisfy a condition of the simplified potential in Eq. (11)). This frequency is well above all position and orientation crossover frequencies we previously measured and modelled for similar particle materials and shapes.[12, 34] We use the same electric field voltage and frequency for all particle shapes to facilitate comparison and contrast of measured and modeled energy landscapes.

Thermally sampled disk particle positions within the nonuniform AC electric field are tracked (**Fig. 2B,C**) to obtain time averaged histograms vs. position relative to the most probable position at the electric field minimum at the electrode gap center (**Fig. 2D**). Particle orientation was not tracked but was assigned randomly to generate landscapes for comparison with other particle shapes (trying to track orientation also produces random orientations since orientation is identified randomly). Boltzmann inversions of the measured histograms yield 2D and 1D potential energy landscapes for the time-averaged dipole-field interactions (**Figs. 2E,F**). The simplified dipole-field potential in Eq. (11) is fit and shown with the measured data (**Figs. 2E,F**) using independently specified material properties, measured particle dimensions, and fit parameters (via nonlinear least squares minimization) in **Tables 1, 2**.

The direct measurements of dipole-field potential energy landscapes for the disk particles show good agreement with the simple model in Eq. (11). Because of disk symmetry, the energy landscape has no orientation dependence and f_θ=0. The fit value of f_x=0.73 is less than a sphere of the same volume, which has f_x=1 as per the definition in Eq. (12) and as confirmed in prior measurements with a similar measurement and analysis.[26-27] The theoretical value for oblate ellipsoids (Eqs. (5), (12)) with: (1) the same radii (but smaller volume) has f_x=0.40, (2) the same volume and relative dimensions (but larger absolute dimensions) has f_x=0.40, (3) the same volume and thickness, a_z (but larger in-plane radii, a_x, a_y) has f_x=0.24, and (4) the same volume and in-plane radii (but larger a_z) has f_x=0.71. We will not perform a similar exhaustive analysis for other shapes in the following, but these results show that even for a simple disk there is not an obvious simple route to an equivalent oblate ellipsoid. However, adding material to an oblate ellipsoid in the z-particle coordinate (*i.e.*, greater a_z) has the greatest similar quantitative effect (fit f_x=0.73 vs. model f_x=0.71) to disks with the same a_x, a_y, which indicates the importance of capturing polarization along the shortest particle axis (*i.e.*, f_x in Eq. (11) replaces $f_{cm,z}$ in Eq. (10)). We proceed to measure and model additional particle shapes to understand semi-empirical trends in fit f_x and f_θ parameters in cases where there is no clear theoretical guidance.

Table 1. Material properties for modeling measured dipole-field potentials (Eq. (11)).

Parameter	Value	Parameter	Value
$\varepsilon_m/\varepsilon_0$[a]	78	d[f] (μm)	100
$\varepsilon_p/\varepsilon_0$[b]	3.2	a_z[f] (μm)	0.85
σ_m[c] (μS/cm)	12.6	h_m[g] (μm)	0.15
σ_p[d] (μS/cm)	110	V_{pp} (V)	3
f_{cm}[e]	-0.3684	ω (MHz)	5

[a]handbook values.[41] [b]manufacturer value. [c]conductivity measurement, consistent with CO_2 saturated deionized H_2O ionic strength. [d]due to electrostatic double layer, based on prior measurements and models.[12, 27] [e]calculated from Eq. (12).[f]laser scanning microscope. [g]prior study.[12, 37]

Table 2. Particle geometric and fit parameters for modeling measured dipole-field potentials (Eq. (11)).

shape	#[a]	a_x/μm[b]	a_y/μm[b]	s	$v_p/\mu m^3$	f_x[c]	f_x[d]	f_θ[c]	f_θ[d]
disk	4	4.0	4.0	1.0	85.4±15	0.73±0.13	0.71	0	0
ellipse	2	4.5	3.5	1.3	84.1±14	0.63±0.12	0.72	0.037±0.007	0.031
ellipse	2	4.0	2.5	1.6	53.4±10	0.64±0.13	0.84	0.075±0.016	0.073
rectangle	2	4.0	3.1	1.3	83.1±15	0.67±0.2	--	0.033±0.009	--
rectangle	3	4.0	2.25	1.8	60.3±12	0.70±0.15	--	0.064±0.014	--
rectangle	3	8.1	2.15	3.8	118±20	0.64±0.13	--	0.108±0.022	--
rectangle	1	5.0	1.15	4.4	38.5±9	0.50±0.16	--	0.113±0.03	--
rhombus	3	4.9	3.45	1.2	67.6±10	0.66±0.12	--	0.041±0.009	--
square	4	4.35	4.35	1.0	127±20	0.51±0.1	--	$3.6\pm0.7\times10^{-4}$	--

[a]particles measured. [b]laser scanning microscope (error ±0.1 μm). [c]fit position (f_x) and orientation (f_θ) factors, error based on v_p error. [d]ellipsoid model (Eq. (12)) f_x and f_θ for equivalent mean volume ellipsoid (see text).

Elliptical Prisms

With an understanding of dipole-field energy landscapes for isotropic disks, we next investigate two aspect ratios of elliptical prisms (a_x=4 μm, $s=a_x/a_y$=1.3, 1.6, a_z=0.85 μm) (**Fig. 3**). Similar to comparing disks with oblate ellipsoids, we also compare elliptical prisms with scalene ellipsoids where $a_x \neq a_y \neq a_z$. At 5 MHz, the particle's longest axis becomes aligned with the dominant field direction (other orientations can be favored at other AC field frequencies depending on shape and material properties[12, 34]). In contrast to tracking only disk positions in **Fig. 2**, for elliptical prisms we now track position and orientation (**Figs. 3B,C**) to produce 2D and 1D histograms and energy landscapes (**Figs. 3D-F**). The resulting measured energy landscape is fit to Eq. (11) using the same parameters in **Tables 1, 2** as the disk, but now with the measured ellipse dimensions and both f_x and f_θ as fit parameters. The measured potential and Eq. (11) show good agreement for s=1.3, 1.6, with s=1.6 results shown in **Figs. 3E,F**. It should be noted that smallest aspect ratio ellipse measured here has a sufficient energy barrier to rotation so that only aligned states are observed.

As elliptical prism aspect ratio is increased, including the disk limit, values of f_θ increase monotonically (**Table 2**) reflecting increasing alignment with the electric field (for particles with the same volume). This observed monotonic trend in f_θ as a function aspect ratio is consistent with the model for scalene ellipsoids (Eqs. (10)-(12)) with the same projected dimensions but equivalent volume via a greater thickness (based on similar analysis of equivalent ellipsoid options discussed in more detail for disk vs. oblate ellipsoids). The fit results for the position dependent factor f_x do not display an obvious trend, at least within the uncertainty of the fit values. Theoretical values for equivalent scalene ellipsoids in **Table 2** suggest a weak trend in f_x, but further discussion is deferred for a collective analysis of additional results for more superelliptical prism shapes.

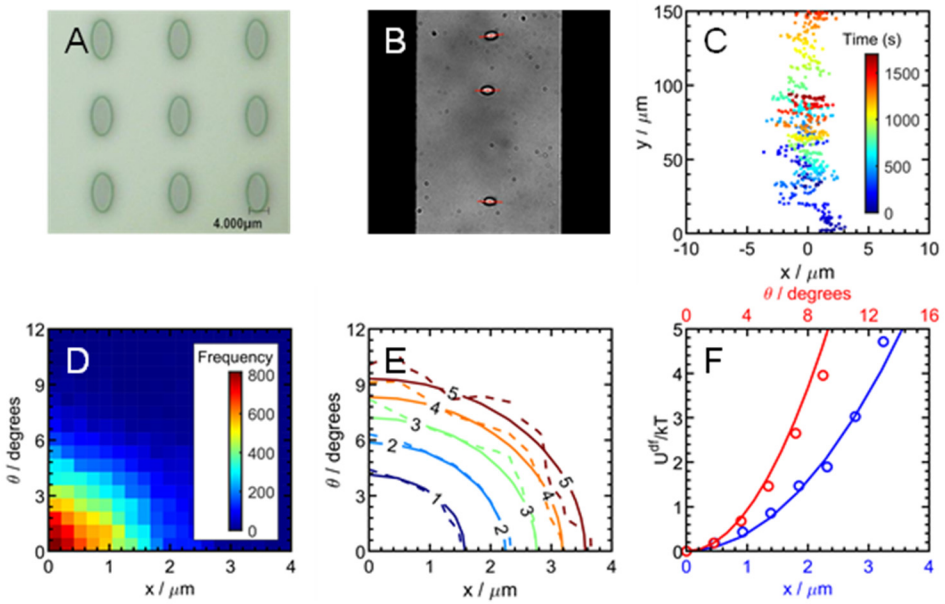

Fig. 3. Elliptical prism particle dipole-field energy landscape. Panel information same as Fig. 2, with abbreviated information, including: **(A)** Particle images (a_x=4 μm, a_y=2.5 μm, a_z=0.85 μm, n=2). **(B)** Video microscopy. **(C)** Particle center trajectories. **(D)** Histogram of (x, θ) distribution. **(E)** Contour plot for (dashed) measured 2D energy landscape and (solid) Eq. (11) with fit f_x, f_θ = parameters in Table 2. **(F)** Projected 1D x (blue), θ (red) landscapes for (points) measurements and (lines) Eq. (11).

Rounded Rectangular Prisms

We next measure and model rounded rectangular (superelliptical) prisms that are anisotropic like ellipses but have corners as a new feature (by adjusting n=2 for ellipses to n=10 for rounded rectangles in Eq. (1), **Fig. 1A**). This particle shape is not obviously well approximated as an ellipsoid, so this provides a test of a novel particle shape dipole-field potential for which theoretical models are not available. Performing the same characterization, particle tracking, and inverse analysis as in the cases of disk and elliptical prism particles, measured energy landscapes were obtained for s=1.29-4.35 with representative results shown for s=1.78 in **Fig. 4**. Measured energy landscapes show good agreement with the model in Eq. (11) with fit values of f_x and f_θ reported in **Table 2**. The semi-empirical form of the potential in Eq. (11) appears well suited to quantitatively capture the kT-scale features in the measured energy landscapes. Other than the two fit coefficients, the rounded rectangular prism volume (Eq. (2)) appears to correctly account for the magnitudes of interactions for different particle sizes and shapes.

For all rounded rectangular prism particle aspect ratios investigated, the most probable and lowest energy orientation is the major axis aligned with the dominant field direction. This behavior is accurately captured by the energy landscape model and is consistent with elliptical prism particles. As with elliptical prisms, all rounded rectangles had sufficient energy barriers to rotation so that only aligned states were observed. Trends in f_x and f_θ vs. aspect ratio are similar for rounded rectangular prisms and elliptical prisms; f_θ increases monotonically with s and f_x is essentially independent, or perhaps weakly decreasing with increasing s, within the fit uncertainty. Given the lack of theoretical guidance on expected trends in the aspect ratio dependence of the positional and orientational energy of non-ellipsoidal particles in AC electric fields, we revisit the trends in f_x and f_θ for superelliptical prism particles after characterizing additional particle shapes.

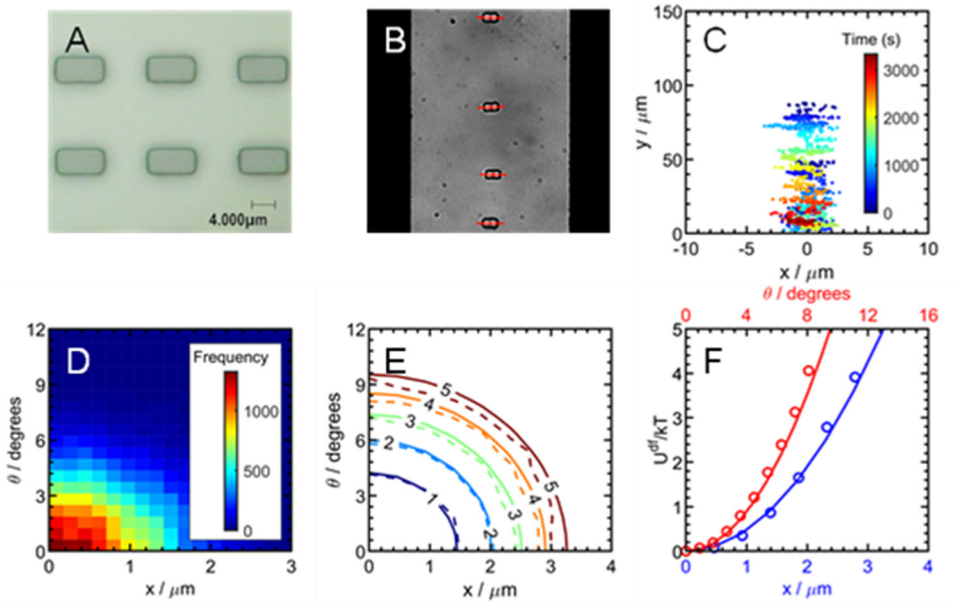

Fig. 4. Rounded rectangular prism particle dipole-field energy landscape. Panel information same as Fig. 2, with abbreviated information, including: **(A)** Particle images (a_x=4 µm, a_y= 2.25 µm, a_z=0.85 µm, n=10). **(B)** Video microscopy. **(C)** Particle center trajectories. **(D)** Histogram of (x, θ) distribution. **(E)** Contour plot for (dashed) measured 2D energy landscape and (solid) Eq. (11) with fit f_x, f_θ = parameters in Table 2. **(F)** Projected 1D x (blue), θ (red) landscapes for (points) measurements and (lines) Eq. (11).

Rounded Rhombus Prisms

In addition to adding corners to ellipses to create rounded rectangles, superellipse shapes include rounded rhombuses by adding corners at the major and minor axis termini (by adjusting n=2 for ellipses to n=1.2 for rounded rhombuses in Eq. (1), see **Fig. 1**). As with anisotropic ellipses and rounded rectangles, the rounded rhombus particles have a most probable and lowest energy orientation with their longest axis aligned with the field. The single aspect ratio rounded rhombuses studied also had sufficient energy barriers to rotation so that only aligned states were observed. Using the same measurement and modeling approaches applied to all shapes reported thus far, the 1D and 2D and dipole-field energy landscapes and fit parameters are reported for a single aspect ratio (**Fig. 5**, **Table 2**). The potential in Eq. (11) with fit f_x and f_θ appears well-suited to quantitatively capture the kT-scale features in the measured energy landscapes with the rounded rhombus prism volume (Eq. (2)) and material properties in f_{cm} (Eq. (12)) accurately accounting for the energy magnitude. Again, without theoretical estimates for rhombus behavior in AC electric fields, we revisit the trends in fit f_x and f_θ for all superelliptical prism particles.

Rounded Square Prisms

The final shape we investigate is rounded square prisms (n=10 in Eq. (1)), which are part of the superellipse shape class (**Fig. 1**), and rounded corners are obtained during particle fabrication due to photolithography resolution limits (**Fig. 6**). While squares are isotropic in the sense that they possess identical orthogonal axes (orthotropic) with unit aspect ratio (s=1), they have corners and orientational symmetry that distinguish them from disks. Using the same measurement and analysis approach applied to all other particle shapes, the rounded squares reveal a new feature compared to other particles; the measured energy landscape has a ~2.5kT rotational barrier (**Figs.**

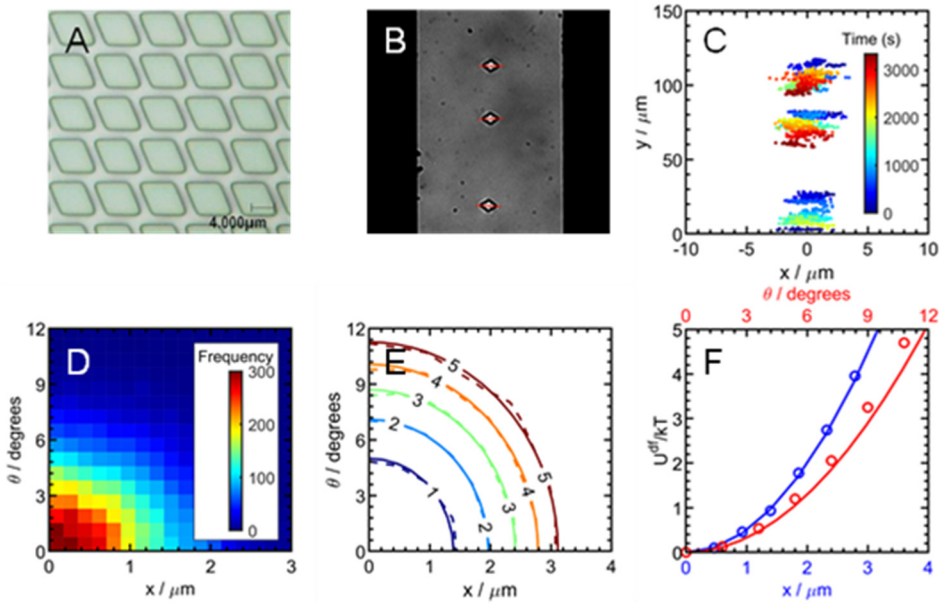

Fig. 5. Rounded rhombus prism particle dipole-field energy landscape. Panel information same as Fig. 2, with abbreviated information, including: **(A)** Particle images (a_x=4.9 μm, a_y=3.35 μm, a_z=0.85 μm, n=1.2). **(B)** Video microscopy. **(C)** Particle center trajectories. **(D)** Histogram of (x, θ) distribution. **(E)** Contour plot for (dashed) measured 2D energy landscape and (solid) Eq. (11) with fit f_x, f_θ = parameters in Table 2. **(F)** Projected 1D x (blue), θ (red) landscapes for (points) measurements and (lines) Eq. (11).

6E,F). The minimum energy state corresponds to squares at the field minimum (x=0) with edges aligned parallel to the electrode edges (perpendicular to the field), which can also be described as the particle's smallest dimension aligned with the field (perpendicular to the electrode edges). An energy barrier maximum is measured at 45 degrees relative to the lowest energy orientation, which corresponds to the square diagonal aligned with the electric field. The other shapes investigated also likely have an orientation dependent energy barrier, but it is too high to be sampled via kT-scale Brownian rotation compared to the rounded square particle.

Given the square symmetry and rotational energy barrier, the model energy landscape in Eq. (11) is modified by letting θ=2θ and fitting f_x and f_θ values reported in **Table 2**. The modelled energy landscape shows good agreement with the measurement with the specified square prism volume (Eq. (2)) and material properties in f_{cm} (Eq. (12)). The value of the fit position dependent parameter, f_x, for squares is similar to all other shapes measured. However, the orientation dependent parameter, f_θ, while being necessarily nonzero to produce the observed orientation dependence, is significantly smaller than all other anisotropic particle shapes (except for the disk where it is identically zero due to its isotropic shape). The square has two obvious characteristic length scales associated with the length of its sides and diagonal, but in contrast to other shapes, the shortest dimension aligned with the field is the minimum energy orientation and the longest dimension aligned with the field has the maximum energy. However, the square diagonal and sides are not orthogonal and do not define an analogous aspect ratio to other shapes and have less clear connections to the depolarization factor (Eq. (6)). Despite differences between squares and other shapes, Eq. (11) accurately captures the measured energy landscape. The fit f_x and f_θ coefficients are analyzed in the following section to further understand how they relate to particle shape.

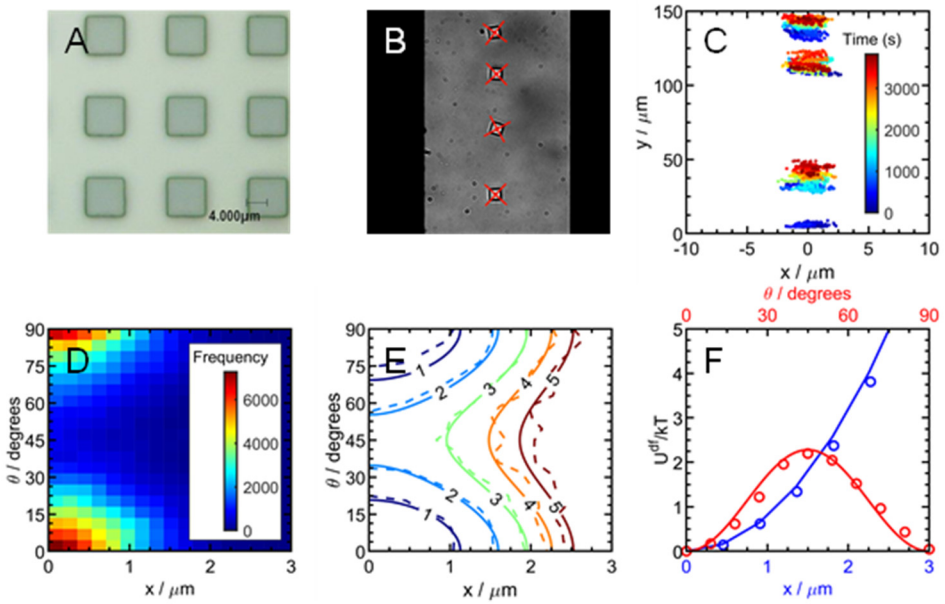

Fig. 6. Rounded square prism particle dipole-field energy landscape. Panel information same as Fig. 2, with abbreviated information, including: **(A)** Particle images (a_x=4.35 μm, a_y=4.35 μm, a_z=0.85 μm, n=10). **(B)** Video microscopy. **(C)** Particle center trajectories. **(D)** Histogram of (x, θ) distribution. **(E)** Contour plot for (dashed) measured 2D energy landscape and (solid) Eq. (11) with fit f_x, f_θ = parameters in Table 2. **(F)** Projected 1D x (blue), θ (red) landscapes for (points) measurements and (lines) Eq. (11).

Simplified Model of Position & Orientation Parameters

Values of f_x and f_θ in Eq. (11) that capture all measured superelliptical prism particle energy landscapes in AC electric fields (**Figs. 2-6**) are summarized in **Table 2**. These tabular values are plotted vs. 1-s^{-1} in **Fig. 7** to show a collapse of fit data within measurement uncertainty to a linear trend for f_θ and constant value for f_x. The scaling contained in the x-axes in **Fig. 7** was obtained semi-empirically by testing functionalities based on the dependence of f_x and f_θ for ellipsoids in Eq. (12) (that do not obviously extend to superelliptical shapes). In brief, the aspect ratio dependence in **Fig. 7** can be understood by considering several approximations. The particle axis-dependent $f_{cm,k}$ values in the ellipsoid theory are approximately proportional to an ellipsoid's principle radii (via the depolarization factor dependence). From the definitions for ellipsoids in Eq. (12), then $f_\theta \propto (a_y - a_x)$ and $f_x \propto a_z$. When this scaling with particle dimensions is

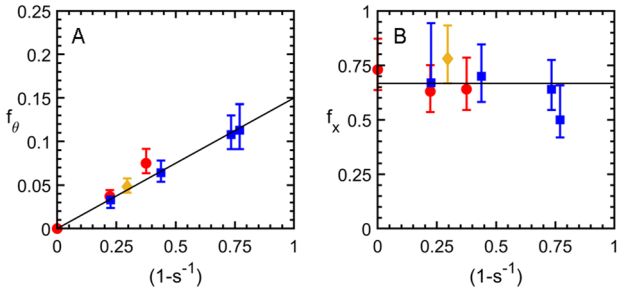

Fig. 7. Orientation and position factors in Eq. (11) for all shapes. Data points are colored to distinguish particle shape by superellipse parameter; red circles (n=2), blue squares (n=10), and yellow diamond (n=1.2). **(A)** Orientation factor data vs. function of aspect ratio with slope=0.15 (black line). **(B)** Position factor data vs. function of aspect ratio with a constant of 2/3 (black line) (mean of values in Table 2).

nondimensionalized by the particle long axis, a_x, the apparent scaling of f_θ as $1\text{-}s^{-1}$ is obtained (**Fig. 7A**), as well as the aspect ratio independence of f_x, since a_z is constant in this work (**Fig. 7B**). In the final analysis, the linear trends capture the fit f_x and f_θ for all particle geometries investigated with the exception of the square (which we revisit below).

Based on these findings, the dipole-field potential energy landscapes for elliptical prisms and anisotropic superelliptical prisms in nonuniform AC electric fields are given by,

$$u^{\mathrm{df}}\left(x,\theta\right) = -P^{\mathrm{df}}\left[0.15\left(1-s^{-1}\right)E_x^2\sin^2\theta + \left(2/3\right)E_z^2\left(x\right)\right] \tag{20}$$

where the position and orientation dependence are a function of only particle aspect ratio and field shape (via its components), and the amplitude, P^{df}, conveniently separates shape dependent particle volume (size) and shape-independent particle and medium material properties. Because the form of Eq. (20) is obtained by simplifying the ellipsoid theory (Eqs. (10)-(12)), it is designed to be accurate for 2D prolate, oblate, and scalene ellipsoids of different volumes and absolute dimensions,[12, 34] including different thicknesses than the particles measured in this work. The expression in Eq. (20) also naturally reduces to the previously validated expression for spherical colloids.[27, 42] Because Eq. (20) captures measured SU-8 particle energy landscapes with independently characterized material properties (dielectric constants, conductivities in **Table 1**), it will also capture previously reported measured potentials for different particle materials, shapes, and sizes at appropriate field conditions (particles aligned at field minimum), including: gold nanoparticles,[40] silica and latex spherical colloids in aqueous and non-aqueous media,[26-27, 42-45] anisotropic SU8 particles,[12, 34] anisotropic silica-gold composite particles,[46] and spherical colloids in multipolar AC electric fields.[10, 13] By validating a simple model potential for different superelliptical prism shaped particles in this work, and ensuring its form remains valid for ellipsoidal and spherical colloids, it is capable of capturing many different particle shapes and materials properties previously validated against the more complex 6-dimensional potential energy function (*i.e.*, Eq. (4)) that is the starting point for the present analytical model.

For the specific case of the rounded squares, the form of Eq. (20) accurately captures the measured energy landscape with two modifications: (1) the orientation dependence is $\sin^2(2\theta)$ to account for minima/maxima every 45 degrees rather than 90 degrees for the other anisotropic particles, and (2) $f_\theta = 0.00036$ instead of $0.15(1\text{-}s^{-1})$ since there is no obvious ratio of characteristic length scales that would yield a suitable estimate for s (*e.g.*, a square diagonal/side lengths = $\sqrt{2}$, which is too high even when considering rounded corners). Based on this finding for rounded square prism particles, a suitable general energy landscape form might exist for N-sided polygonal prism particles and their rounded variants in terms of orientation dependent maxima/minima, but without additional data, we limit speculation on further details.

Ultimately, the simple model in Eq. (20) accurately quantifies all of the energy landscape features for elliptical and superelliptical prism shaped particles in nonuniform AC electric fields at frequencies when particles exist in quasi-2D states localized at electric field minima and aligned with the dominant field direction. Similar simplified forms can likely be developed for particles in which different field conditions produce different minimum energy positions and orientations,[12, 34] and for particles with other symmetries that exhibit different orientation dependences.

Conclusions

We reported direct measurements and new accurate simple models of dipole-field energy landscapes of photolithographically fabricated colloidal particles in nonuniform AC electric fields. To understand roles of particle aspect ratio and corner features, superelliptical prism particle shapes were systematically varied by changing anisotropy from disks to ellipses and tuning corner curvature to include squares, rhombuses, and rectangles. Optical microscopy was used to monitor the equilibrium thermal sampling of position and orientation of particles sedimented onto glass microscope slides within high frequency AC electric fields between coplanar electrodes. By directly and non-intrusively measuring time-averaged histograms of equilibrium thermal sampling of particle positions and orientations, *kT*-scale dipole-field energy landscapes for each particle shape are obtained via Boltzmann inversions with no additional assumptions. This approach to non-intrusive measurement and analysis of systematically varying particle shapes in nonuniform AC electric fields has not been previously investigated to the authors' knowledge.

With direct sensitive measurements of unique dipole-field energy landscapes for each particle shape, we develop a simple analytical model that captures all observed features. We first simplify a 6D model for ellipsoids to quasi-2D configurations, and then make assumptions that permit a form suitable for superelliptical prism shaped particles. By allowing two adjustable parameters that quantify the relative amplitudes of orientational and positional energies, the simple energy landscape model captures all measured energy landscapes within measurement uncertainty. Upon further analysis of the two adjustable parameters, the orientational factor is found to have a simple scaling with the particle aspect ratio and the position factor is shape invariant.

The final energy landscape functional form accounts for particle shape, size, and material properties in separate terms suggesting its predictive capability for diverse particle systems, provided assumptions regarding applicable conditions are satisfied. Given that dipole-dipole interactions correspond to a single dipole interacting with the field of an adjacent dipole, the simple dipole-field potential in this work also suggests opportunities to further simplify dipolar potentials (in connection to our previous simplifications of anisotropic particle dipolar potentials[37]). Ultimately, the measured and modelled dipole-field energy landscapes can be used to analyze, simulate, design, control, and optimize electric field mediated behavior and properties of diverse natural and synthetic colloidal particles.

Conflicts of interest

There are no conflicts to declare.

Acknowledgments

We acknowledge financial support by the National Science Foundation CBET 2113594.

Reference

1. Parsegian, V. A. *Van Der Waals Forces*. Cambridge University Press: Cambridge, **2005**.
2. Cole, M. W.; Velegol, D.; Kim, H.-Y.; Lucas, A. A. Nanoscale Van Der Waals Interactions. *Molecular Simulation* **2009,** *35*, 849-866.
3. Kwaadgras, B. W.; van Roij, R.; Dijkstra, M. Self-Consistent Electric Field-Induced Dipole Interaction of Colloidal Spheres, Cubes, Rods, and Dumbbells. *The Journal of Chemical Physics* **2014,** *140*, 154901.
4. Ashkin, A.; Dziedzic, J. M.; Bjorkholm, J. E.; Chu, S. Observation of a Single-Beam Gradient Force Optical Trap for Dielectric Particles. *Optics Letters* **1986,** *11*, 288-290.

5. Gosse, C.; Croquette, V. Magnetic Tweezers: Micromanipulation and Force Measurement at the Molecular Level. *Biophysical Journal* **2002,** *82*, 3314-3329.
6. Edwards, B.; Engheta, N.; Evoy, S. Electric Tweezers: Experimental Study of Positive Dielectrophoresis-Based Positioning and Orientation of a Nanorod. *Journal of Applied Physics* **2007,** *102*, 024913.
7. Fan, D. L.; Zhu, F. Q.; Cammarata, R. C.; Chien, C. L. Electric Tweezers. *Nano Today* **2011,** *6*, 339-354.
8. Sarkar, R.; Rybenkov, V. V. A Guide to Magnetic Tweezers and Their Applications. *Frontiers in Physics* **2016,** *4*.
9. Polimeno, P.; Magazzù, A.; Iatì, M. A.; Patti, F.; Saija, R.; Esposti Boschi, C. D.; Donato, M. G.; Gucciardi, P. G.; Jones, P. H.; Volpe, G.; Maragò, O. M. Optical Tweezers and Their Applications. *Journal of Quantitative Spectroscopy and Radiative Transfer* **2018,** *218*, 131-150.
10. Zhang, J.; Zhang, Y.; Bevan, M. A. Spatially Varying Colloidal Phase Behavior on Multi-Dimensional Energy Landscapes. *J. Chem. Phys.* **2020,** *152*, 054905.
11. Chen, H.-C.; Cheng, C.-J. Holographic Optical Tweezers: Techniques and Biomedical Applications. *Applied Sciences* **2022,** *12*, 10244.
12. Rupp, B.; Torres-Diaz, I.; Hua, X.; Bevan, M. A. Measurement of Anisotropic Particle Interactions with Nonuniform Ac Electric Fields. *Langmuir* **2018,** *34*, 2497-2504.
13. Zhang, J.; Yang, J.; Zhang, Y.; Bevan, M. A. Controlling Colloidal Crystals Via Morphing Energy Landscapes and Reinforcement Learning. *Science Advances* **2020,** *6*, eabd6716.
14. Su, H.-W.; Prieto, J. L.; Voldman, J. Rapid Dielectrophoretic Characterization of Single Cells Using the Dielectrophoretic Spring. *Lab on a Chip* **2013,** *13*, 4109-4117.
15. Kralj, J. G.; Lis, M. T. W.; Schmidt, M. A.; Jensen, K. F. Continuous Dielectrophoretic Size-Based Particle Sorting. *Analytical Chemistry* **2006,** *78*, 5019-5025.
16. Bharti, B.; Velev, O. D. Assembly of Reconfigurable Colloidal Structures by Multidirectional Field-Induced Interactions. *Langmuir* **2015,** *31*, 7897-7908.
17. Jones, T. B. *Electromechanics of Particles*. Cambridge University Press: Cambridge, **1995**; p 265.
18. Morgan, H.; Green, N. G. *Ac Electrokinetics: Colloids and Nanoparticles*. Research Studies Press: Philadelphia, PA, **2003**.
19. Pethig, R. *Dielectrophoresis: Theory, Methodology, and Biological Applications*. John Wiley & Sons, Incorporated: **2017**.
20. Stratton, J. A. *Electromagnetic Theory*. McGraw-Hill Book Company, Inc.: New York, **1941**; p 615.
21. O'Konski, C. T. Electric Properties of Macromolecules. V. Theory of Ionic Polarization in Polyelectrolytes. *Journal of Physical Chemistry* **1960,** *64*, 605-619.
22. Saville, D. A.; Bellini, T.; Degiorgio, V.; Mantegazza, F. An Extended Maxwell--Wagner Theory for the Electric Birefringence of Charged Colloids. *J. Chem. Phys.* **2000,** *113*, 6974-6983.
23. Zhou, H.; Preston, M. A.; Tilton, R. D.; White, L. R. Calculation of the Electric Polarizability of a Charged Spherical Dielectric Particle by the Theory of Colloidal Electrokinetics. *Journal of Colloid and Interface Science* **2005,** *285*, 845-856.
24. Sasanpour, M.; Azadbakht, A.; Mollaei, P.; Reihani, S. N. S. Proper Measurement of Pure Dielectrophoresis Force Acting on a Rbc Using Optical Tweezers. *Biomed. Opt. Express* **2019,** *10*, 5639-5649.
25. Pesce, G.; Rusciano, G.; Zito, G.; Sasso, A. Simultaneous Measurements of Electrophoretic and Dielectrophoretic Forces Using Optical Tweezers. *Optics Express* **2015,** *23*, 9363-9368.
26. Juarez, J. J.; Bevan, M. A. Interactions and Microstructures in Electric Field Mediated Colloidal Assembly. *J. Chem. Phys.* **2009,** *131*, 134704.
27. Juarez, J. J.; Cui, J.-Q.; Liu, B. G.; Bevan, M. A. Kt-Scale Colloidal Interactions in High Frequency Inhomogeneous Ac Electric Fields. I. Single Particles. *Langmuir* **2011,** *27*, 9211-9218.
28. Smith, B. D.; Fichthorn, K. A.; Kirby, D. J.; Quimby, L. M.; Triplett, D. A.; González, P.; Hernández, D.; Keating, C. D. Asymmetric Van Der Waals Forces Drive Orientation of Compositionally Anisotropic Nanocylinders within Smectic Arrays: Experiment and Simulation. *ACS Nano* **2014,** *8*,

657-670.
29. Behdani, B.; Wang, K.; Silvera Batista, C. A. Electric Polarizability of Metallodielectric Janus Particles in Electrolyte Solutions. *Soft Matter* **2021,** *17*, 9410-9419.
30. Miller, R. D.; Jones, T. B. Electro-Orientation of Ellipsoidal Erythrocytes. Theory and Experiment. *Biophysical Journal* **1993,** *64*, 1588-1595.
31. Bitter, J. L.; Yang, Y.; Duncan, G.; Fairbrother, H.; Bevan, M. A. Interfacial and Confined Colloidal Rod Diffusion. *Langmuir* **2017,** *33*, 9034-9042.
32. Yang, Y.; Bevan, M. A. Interfacial Colloidal Rod Dynamics: Coefficients, Simulations, and Analysis. *The Journal of Chemical Physics* **2017,** *147*, 054902.
33. Keh, H. J.; Anderson, J. L. Boundary Effects on Electrophoretic Motion of Colloidal Spheres. *J. Fluid Mech.* **1985,** *153*, 417-439.
34. Torres-Díaz, I.; Rupp, B.; Yang, Y.; Bevan, M. A. Energy Landscapes for Ellipsoids in Non-Uniform Ac Electric Fields. *Soft Matter* **2018,** *14*, 934-944.
35. Beckham, R. E.; Bevan, M. A. Interfacial Colloidal Sedimentation Equilibrium I. Intensity Based Confocal Microscopy. *J. Chem. Phys.* **2007,** *127*, 164708.
36. Morgan, H.; García Izquierdo, A.; Bakewell, D.; Green, N. G.; Ramos, A. The Dielectrophoretic and Travelling Wave Forces Generated by Interdigitated Electrode Arrays: Analytical Solution Using Fourier Series. *Journal of Physics D: Applied Physics* **2001,** *34*, 1553-1561.
37. Hendley, R. S.; Torres-Díaz, I.; Bevan, M. A. Anisotropic Colloidal Interactions & Assembly in Ac Electric Fields. *Soft Matter* **2021,** *17*, 9066-9077.
38. Hendley, R. S.; Zhang, L.; Bevan, M. A. Design Rules for 2d Field Mediated Assembly of Different Shaped Colloids into Diverse Microstructures. *Soft Matter* **2022,** *18*, 9273-9282.
39. Hernandez, C. J.; Mason, T. G. Colloidal Alphabet Soup: Monodisperse Dispersions of Shape-Designed Lithoparticles. *The Journal of Physical Chemistry C* **2007,** *111*, 4477-4480.
40. Bahukudumbi, P.; Everett, W. N.; Beskok, A.; Huff, G. H.; Lagoudas, D.; Ounaies, Z.; Bevan, M. A. Colloidal Microstructures, Transport, and Impedance Properties within Interfacial Microelectrodes. *Appl. Phys. Lett.* **2007,** *90*, 224102.
41. Lide, D. R. *Crc Handbook of Chemistry and Physics*. CRC Press: New York, **2000**; Vol. 80.
42. Juarez, J. J.; Liu, B. G.; Cui, J.-Q.; Bevan, M. A. Kt-Scale Colloidal Interactions in High-Frequency Inhomogeneous Ac Electric Fields. Ii. Concentrated Ensembles. *Langmuir* **2011,** *27*, 9219-9226.
43. Juarez, J. J.; Bevan, M. A. Feedback Controlled Colloidal Self-Assembly. *Adv. Funct. Mater.* **2012,** *22*, 3833-3839.
44. Juarez, J. J.; Feicht, S. E.; Bevan, M. A. Electric Field Mediated Assembly of Three Dimensional Equilibrium Colloidal Crystals. *Soft Matter* **2012,** *8*, 94-103.
45. Juarez, J. J.; Mathai, P. P.; Liddle, J. A.; Bevan, M. A. Multiple Electrokinetic Actuators for Feedback Control of Colloidal Crystal Size. *Lab Chip* **2012,** *12*, 4063-4070.
46. Famularo, N. R.; Hendley, R. S.; Boehm, S. J.; Guo, X.; Mayer, T. S.; Bevan, M. A.; Keating, C. D. Segmentation-Dependent Dielectrophoretic Assembly of Multisegment Metal/Dielectric Particles. *The Journal of Physical Chemistry C* **2020,** *124*, 18755-18769.

For Table of Contents Use Only

(1.75 in. high and 3.25 in. wide)